

Solid shell prism elements based on hierarchical, heterogeneous, and anisotropic shape functions

Lukasz Kaczmarczyk^{*a}, Hoang Nguyen^a, Zahur Ullah^b, Mebratu Wakeni^a, Chris Pearce^a

^a*Glasgow Computational Engineering Centre, James Watt School of Engineering, University of Glasgow, Glasgow, G12 8QQ, UK*

^b*Advanced Composites Research Group, School of Mechanical and Aerospace Engineering, Queen's University Belfast, Belfast, BT9 5AH, UK*

Abstract

The formulation of a new prism finite element is presented for the nonlinear analysis of solid shells subject to large strains and large displacements. The element is based on hierarchical, heterogeneous, and anisotropic shape functions. As with other solid shell formulations, only displacement degrees of freedom are required to describe the shell kinematics and general three-dimensional material laws can be adopted. However, the novelty of this formulation is the ability to capture complex shell behaviour and avoid locking phenomena, without the need to use reduced integration or adopt additional natural strain or enhanced strain fields. Thus, this element is ideally suited for geometrically and physically nonlinear problems. This is achieved by constructing independent approximation shape functions on both the prism element's triangular faces and through the thickness, where the latter is associated with a local coordinate system that convects with deformation of the shell. The element is extremely efficient, with the hierarchical property lending itself to an efficient and highly scalable multigrid solver, and the heterogeneity property enables local p-adaptivity. The paper demonstrates performance of the element for a number of linear and geometrically nonlinear problems, benchmarked against well established problems in the literature. The formulation has been implemented in the MoFEM library [1]. Both the code and the data for the numerical examples are open-source [2].

Keywords: hierarchical shape functions, prism element, solid shell finite element, large deformations, multi-grid

1. Introduction

Shell structures continue to generate scientific interest and represent an ongoing challenge in terms of computational mechanics. Shells are typically thin, curved and lightweight structures, and are technically important across a range of applications, including civil and structural engineering, aerospace, automotive, industrial processing and marine. There is also a growing interest in the mechanics of shells at the interface of engineering and the life-sciences, where they occur as natural structures comprised of complex materials with unusual nonlinear behaviour.

Degenerated shell theory has been a successful approach for modelling shells for several decades and has worked well for many cases. However, there are a number of restrictions and scenarios where it is less effective. The kinematic assumptions and the rotational degrees of freedom can lead to difficulties. Although in-plane stresses and transverse shear stresses are considered, the stretching effect in the through-thickness direction is not taken into account. Consequently, it is necessary to reduce the general three-dimensional material law to the plane stress condition. When describing the boundary conditions for geometrically nonlinear problems, it is necessary to undertake a complex update of the rotations. Problems also arise when shell elements are used in combination with solid elements. Therefore, it is desirable to have an alternative approach that is able to overcome these shortcomings.

Solid shell theory [3, 4] assumes the element has only displacement DOFs. As a result, these elements are capable of connecting naturally with continuum elements and overcome the disadvantages related to boundary conditions that are inherent in degenerated shell elements. There is a well-established body of work on the linear and nonlinear analyses of shells using solid shell theory. Hosseini et al. [5] employed it for nonlinear analysis where the isogeometric formulation was used to construct the shell's mid-surface and linear Lagrange function for the approximation through the thickness. Leonetti et al. [6] also worked on the isogeometric implementation of a solid shell element for geometrically nonlinear problem where a generalised constitutive matrix is employed. Solid shell elements also find applications in modelling laminated composites and delamination phenomenon [7, 8, 9, 10].

Despite the advantages of solid shell formulations, locking phenomena, such as shear locking, membrane locking, and especially volumetric and thickness locking, are common problems [11, 12]. There has been considerable efforts to circumvent these by means of assumed natural strain, enhanced assumed strain, and mixed stress-displacement formulations. For example, in order to overcome thickness and volumetric locking, a hybrid-stress formulation was employed [13]. Reese et al. [14] proposed a brick element formulation with the combination of reduced integration and stabilisation concept for large deformation problems based on the enhanced strain method. Later, Reese [15] also proposed an eight-node solid element with reduced integration based on hourglass stabilisation for static problems. Schwarze and Reese [16, 17] developed a reduced integration eight-node solid-shell finite element, requiring only one integration point within the shell plane and at least two integration points through the thickness. The formulation has the advantage of being able to choose an arbitrary number of integration points through the shell thickness and only one enhanced degree-of-freedom is needed to avoid volumetric and thickness locking. The assumed natural strain concept is adopted to avoid shear and curvature thickness locking.

In the present study, a new solid shell prism element is proposed. Independent approximation shape functions are constructed on the triangular faces and through the thickness of the prism element, where the latter is associated with a local coordinate system that convects with deformation of the shell. This anisotropic property of the shape functions avoids locking, without the need to use an assumed strain field or enhanced assumed strain field, or to use reduced integration. Moreover, the prism element is constructed using hierarchical and heterogeneous shape functions, enabling local p -refinement and development of a multigrid solver [18], that means the element is also computationally efficient.

The outline of this paper is as follows. Section 2 presents the framework to construct hierarchical approximations for triangular prism elements and Section 3 discusses the kinematics and linearisation following the solid shell theory. The geometry and displacement approximations and discretisations are given in Section 4. Section 5 evaluates the convergence properties, as well as presenting some benchmark examples of shells with large deformations. Concluding remarks are presented in Section 6.

2. Construction of hierarchical shape functions for prism elements

This section presents the construction of the shape function for the proposed solid shell prism element, shown in Fig. 1. This approximation is hierarchical, heterogeneous, and anisotropic. The hierarchy of the approximation is built on different geometrical entities, i.e. vertices, edges, faces, and volume. Meanwhile, an arbitrary order of approximation can be established independently for each geometrical entity, including each prism, enabling heterogeneous approximations across a finite element mesh. Moreover, approximations functions on the triangular faces are defined independently from those of the quadrilateral faces.

The starting point for construction of the element is the *primary basis* from a set of one-dimensional polynomials $\{\psi_\ell : \ell = 0, 1, \dots\}$ that constitute a hierarchic basis on a reference interval $[-1, 1]$ [19]. The function ψ_ℓ is usually in the form of Legendre polynomial L_ℓ with degree ℓ which are defined as follows

$$L_0(s) = 1, \quad L_1(s) = s, \quad L_{\ell+1}(s) = \frac{2\ell+1}{\ell+1}sL_\ell(s) - \frac{\ell}{\ell+1}L_{\ell-1}(s), \quad s \in [-1, 1], \quad \ell = 1, 2, \dots \quad (1)$$

It is worth noting that a more general form of Legendre polynomials presented here, such as Gegenbauer polynomials, can be found in the literature [20, 19].

A prism element consists of coordinate points (ξ, η, ζ) such that $0 \leq \xi, \eta, \zeta \leq 1$ and $\xi + \eta \leq 1$. In other words, an element is the Cartesian product of a triangle element with coordinates (ξ, η) and a one-dimensional segment element identified by coordinate ζ . Thus, barycentric coordinates λ_j ($j = 0, 1, 2$) of a triangle and affine coordinates μ_i ($i = 0, 1$) of a one-dimensional segment are defined as follows

$$\lambda_0 = 1 - \xi - \eta, \quad \lambda_1 = \xi, \quad \lambda_2 = \eta, \quad (2a)$$

$$\mu_0 = 1 - \zeta, \quad \mu_1 = \zeta, \quad (2b)$$

and their gradient with respect to the Cartesian coordinates (ξ, η, ζ) given by

$$\nabla\lambda_0 = \begin{pmatrix} -1 \\ -1 \\ 0 \end{pmatrix}, \quad \nabla\lambda_1 = \begin{pmatrix} 1 \\ 0 \\ 0 \end{pmatrix}, \quad \nabla\lambda_2 = \begin{pmatrix} 0 \\ 1 \\ 0 \end{pmatrix}, \quad (3a)$$

$$\nabla\mu_0 = \begin{pmatrix} 0 \\ 0 \\ -1 \end{pmatrix}, \quad \nabla\mu_1 = \begin{pmatrix} 0 \\ 0 \\ 1 \end{pmatrix}. \quad (3b)$$

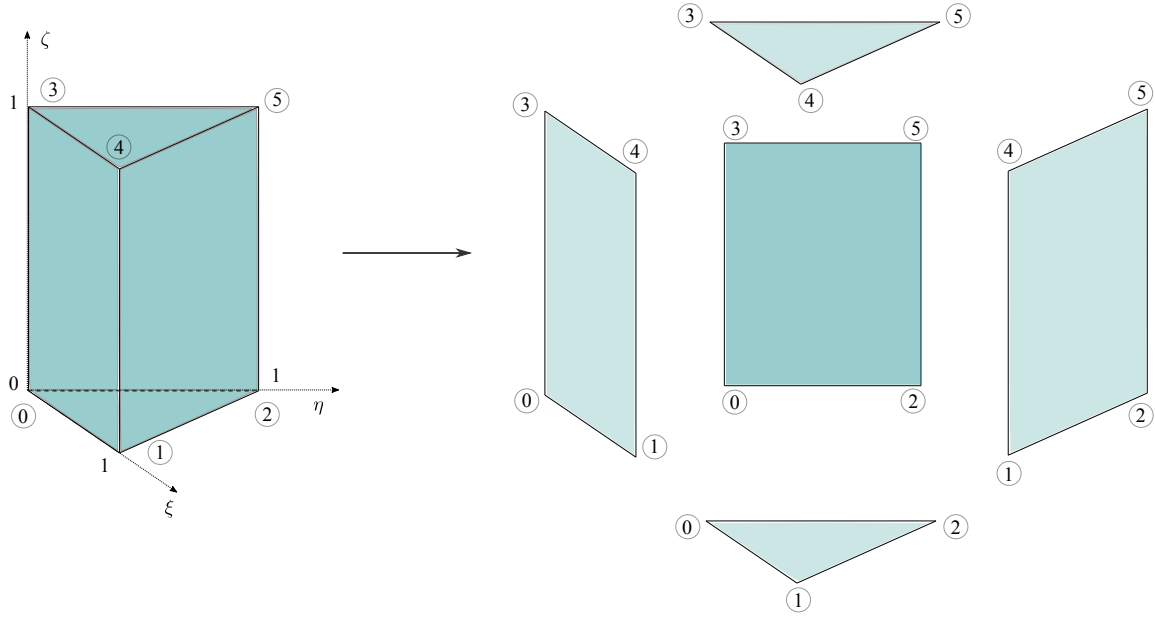


Figure 1: Geometry of prism element and exploded view with node numbering in circles.

2.1. Vertex shape functions

The shape function for a given vertex v ($v=0, \dots, 5$), see Fig. 1, is a bi-linear polynomial that takes the value of one at the vertex to which it is associated and zero at the other vertices. This, together with the fact that it is linear along edges, is sufficient to satisfy the necessary C^0 -continuity of the global vertex functions on adjacent prism elements that share the vertex. Thus the shape function ϕ^v is expressed as the product of the triangle's barycentric coordinates and the segment's affine coordinates as follows

$$\phi^v = \lambda_i \mu_j, \quad (4)$$

where the relationship between the indices v, i and j is given in Table 1

Table 1: Relationship between the indices of the vertex shape functions

v	i	j
0	0	0
1	1	0
2	2	0
3	0	1
4	1	1
5	2	1

2.2. Edge shape functions

There are two types of edges to be considered: triangle edges and through-thickness edges. The Lagrange polynomials given by Eq. (1) are used to define the shape functions

for both of these.

Consider first the triangle edges of the prism's top and bottom triangular faces. The Lagrange polynomials are mapped to an edge with the interval $[-1, 1]$ using the difference of the barycentric coordinates as $L_\ell(\lambda_j - \lambda_k)$. Care must be taken to use the global (rather than local) number ordering of the edge, since edges that are shared by adjacent prism elements may have different local numbering. For example, if the local and global number ordering of Edge 0-1 are the same, then the mapping $\lambda_1 - \lambda_0$ is used, otherwise the difference is reversed.

The shape function for any edge is non-zero on the edge to which it is associated and zero on all other edges. For Edge 0-1, for example, the function $\mu_0\lambda_0\lambda_1$ satisfies this property. Hence, assuming the same local and global numbering, the shape functions associated with edge k - j are

$$\phi_\ell^{\text{te}} = \beta_{ijk}^{\text{te}} L_\ell(\lambda_j - \lambda_k), \quad (5)$$

where $\beta_{ijk}^{\text{te}} = \mu_i\lambda_j\lambda_k$ and the relationship between indices is given in Table 2. $\ell = 0, \dots, p-2$, where p is overall polynomial order of the prism. The gradients of ϕ_ℓ^{te} with respect to (ξ, η, ζ) are given as

$$\begin{aligned} \nabla\phi_\ell^{\text{te}} = & \nabla\mu_i\lambda_j\lambda_k L_\ell(\lambda_j - \lambda_k) + \\ & \mu_i\nabla\lambda_j\lambda_k L_\ell(\lambda_j - \lambda_k) + \\ & \mu_i\lambda_j\nabla\lambda_k L_\ell(\lambda_j - \lambda_k) + \\ & \mu_i\nabla\lambda_j\lambda_k L'_\ell(\lambda_j - \lambda_k) [\nabla\lambda_j - \nabla\lambda_k]. \end{aligned} \quad (6)$$

Table 2: Relationship between indices for triangle edge shape functions

te	i	j	k
0-1	0	1	0
1-2	0	2	1
2-0	0	0	2
3-4	1	1	0
4-5	1	2	1
5-3	1	0	2

The through-thickness edges of the prism's quadrilateral faces are parameterised by the affine coordinates, such that the shape function is expressed as

$$\phi_\ell^{\text{qe}} = \beta_i^{\text{qe}} L_\ell(\mu_1 - \mu_0), \quad (7)$$

where $\ell = 0, \dots, p-2$ and the index i takes values 0, 1, and 2 for Edges 0-3, 1-4, and 2-5, respectively. The Lagrange polynomials L_ℓ have been mapped using the affine coordinates and function $\beta_i^{\text{qe}} = \lambda_i\mu_0\mu_1$ is non-zero on the edge under consideration and zero on all other edges. As above, it has been assumed the local and global number ordering are the same.

2.3. Face shape functions

The prism element comprises two types of faces: triangular and quadrilateral. Following a similar approach to edges, the shape functions for triangular faces are expressed as

$$\phi_{k\ell}^{\Delta} = \beta_i^{\Delta} L_k(\lambda_1 - \lambda_0) L_{\ell}(\lambda_2 - \lambda_0), \quad (8)$$

where $\beta_i^{\Delta} = \mu_i \lambda_0 \lambda_1 \lambda_2$ is selected to enforce the condition that $\phi_{k\ell}^{\Delta}$ is non-zero on the face to which it is associated and zero on all other faces. The index i takes the value of 0 and 1 for Triangles 0-1-2 and 3-4-5, respectively.

For quadrilateral faces, the shape functions are expressed as

$$\phi_{k\ell}^{\square} = \beta_{ij}^{\square} L_k(\mu_1 - \mu_0) L_{\ell}(\lambda_j - \lambda_i), \quad (9)$$

where $\beta_{ij}^{\square} = \mu_0 \mu_1 \lambda_i \lambda_j$ and the relationship between the indices are given in Table 3.

Table 3: Relationship between indices for quadrilateral face shape functions

\square	i	j
0-1-4-3	0	1
1-2-5-4	1	2
2-0-3-5	2	0

2.4. Volume shape functions

To construct the volume shape functions, the hierarchical Lagrange polynomials adopted for the triangular faces in Eq. (8) are expanded through the thickness of the element using the Lagrange polynomials adopted for the quadrilateral edges in Eq. (7). Thus,

$$\phi_{klm}^{\text{P}} = \beta^{\text{P}} L_k(\mu_1 - \mu_0) L_{\ell}(\lambda_1 - \lambda_0) L_m(\lambda_2 - \lambda_0). \quad (10)$$

where $\beta^{\text{P}} = \mu_0 \mu_1 \lambda_0 \lambda_1 \lambda_2$ enforces the condition that the volume shape function is zero on all faces.

It will be shown in the next section of this paper that displacement DOFs associated with triangle edges and faces are expressed in the global Cartesian coordinate system, whereas DOFs associated with quadrilateral edges and faces, and prism volumes are expressed in the local, curvilinear, through-thickness coordinate system. This local coordinate system convects with deformation of the shell. The distribution of DOFs is summarised in Table 4.

To conclude this section, it is worth noting that the proposed shape functions enable significant flexibility in building approximations across a finite element mesh. The heterogeneous property allows different polynomial orders to be applied for different entities at different parts of the mesh. The anisotropic property enables different orders to be used in different directions, e.g. on the top and bottom surfaces or in the through-thickness direction. Furthermore, the hierarchic nature of the shape functions supports effective implementation of a multi-grid solver, which significantly improves the analysis speed due to its inherent scalability.

Table 4: DOFs distribution in different coordinate systems

DOFs	Coordinate system	
	Global Cartesian	Local curvilinear
Vertices	✓	
Edges (triangle)	✓	
Triangles	✓	
Edges (quadrilateral)		✓
Quadrilaterals		✓
Volume		✓

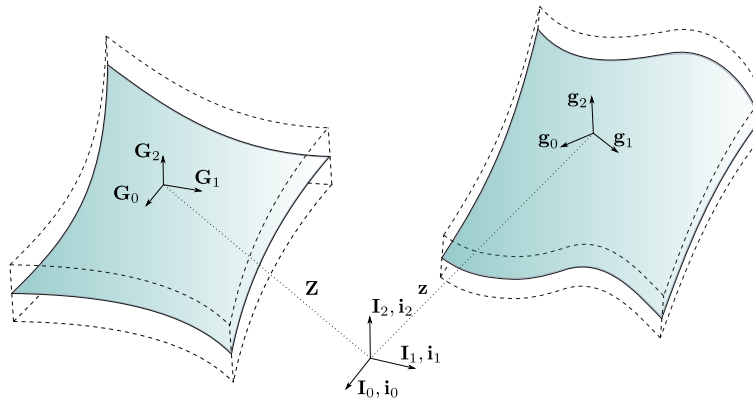


Figure 2: Shell in reference (left) and current (right) configurations.

3. Kinematics of solid shells

Fig. 2 shows the reference (undeformed) and current (deformed) configurations of a shell. The position \mathbf{Z} of a material point in the reference configuration can be expressed as a function of the local curvilinear coordinates $\boldsymbol{\xi} = [\xi, \eta, \zeta]$ and spatially varying thickness ${}^M a(\xi, \eta)$ as follows

$$\mathbf{Z}(\xi, \eta, \zeta) = {}^M \mathbf{Z}(\xi, \eta) + \left(\zeta - \frac{1}{2}\right) {}^M a(\xi, \eta) \mathbf{D}(\xi, \eta), \quad (11)$$

where superscript ${}^M(\cdot)$ indicates the field is defined only on the shell's mid-surface. Meanwhile, ${}^M \mathbf{Z}$ is the projection of the point \mathbf{Z} on the mid-surface and \mathbf{D} represents the normal direction vector in the reference configuration which can be defined as follows

$${}^M \mathbf{Z}(\xi, \eta) = \frac{1}{2} [\mathbf{Z}_u(\xi, \eta) + \mathbf{Z}_\ell(\xi, \eta)], \quad (12a)$$

$$\mathbf{D}(\xi, \eta) = \frac{1}{2} [\mathbf{Z}_u(\xi, \eta) - \mathbf{Z}_\ell(\xi, \eta)], \quad (12b)$$

where \mathbf{Z}_u and \mathbf{Z}_ℓ are the position vectors of a point at the top and bottom surfaces in the reference configuration, respectively. The element kinematics is based on the linear combination of the position of the top and bottom surfaces of the element [5].

In the current configuration the position vector can be expressed as

$$\mathbf{z}(\xi, \eta, \zeta) = {}^M \mathbf{z}(\xi, \eta) + \left(\zeta - \frac{1}{2}\right) {}^M a(\xi, \eta) \mathbf{d}(\xi, \eta), \quad (13)$$

where ${}^M \mathbf{z}$ is the projection of the point on the mid-surface and \mathbf{d} denotes the normal direction vector in the current configuration. These are calculated as follows

$${}^M \mathbf{z}(\xi, \eta) = \frac{1}{2} [\mathbf{z}_u(\xi, \eta) + \mathbf{z}_\ell(\xi, \eta)], \quad (14a)$$

$$\mathbf{d}(\xi, \eta) = \frac{1}{2} [\mathbf{z}_u(\xi, \eta) - \mathbf{z}_\ell(\xi, \eta)]. \quad (14b)$$

Consequently, the position of a point in the current configuration is expressed in terms of its position in the reference configuration and its displacement $\mathbf{u}(\xi, \eta, \zeta)$ as follows

$$\mathbf{z}(\xi, \eta, \zeta) = \mathbf{Z}(\xi, \eta, \zeta) + \mathbf{u}(\xi, \eta, \zeta). \quad (15)$$

By assuming the thickness is uniform throughout the shell in the reference configuration, the covariant base vectors of a material point in the reference configuration can be obtained as follows

$$\mathbf{G}_\alpha = \frac{\partial \mathbf{Z}}{\partial \boldsymbol{\xi}^\alpha} = \frac{\partial {}^M \mathbf{Z}}{\partial \boldsymbol{\xi}^\alpha} + a \left(\zeta - \frac{1}{2}\right) \frac{\partial \mathbf{D}}{\partial \boldsymbol{\xi}^\alpha}, \quad \alpha = 0, 1, \quad (16a)$$

$$\mathbf{G}_2 = a \mathbf{D}, \quad (16b)$$

where $\boldsymbol{\xi}^\alpha$ are basis vectors in the element's reference coordinates.

Similarly, the covariant basis vectors in the current configuration are derived from the partial derivatives of the position vector with respect to curvilinear coordinates $\boldsymbol{\xi}$ as follows

$$\mathbf{g}_\alpha = \frac{\partial \mathbf{z}}{\partial \boldsymbol{\xi}^\alpha} = \mathbf{G}_\alpha + \frac{\partial \mathbf{u}}{\partial \boldsymbol{\xi}^\alpha}, \quad (17a)$$

$$\mathbf{g}_2 = \mathbf{G}_2 + \frac{\partial \mathbf{u}}{\partial \zeta}. \quad (17b)$$

Consequently, the coefficients of the metric tensors in the reference and current configurations are defined as

$$G^{AB} = \mathbf{G}_A \cdot \mathbf{G}_B, \quad (18a)$$

$$g_{ab} = \mathbf{g}_a \cdot \mathbf{g}_b. \quad (18b)$$

The relation between the covariant and contravariant basis vectors in the reference and current configurations are expressed as follows

$$\mathbf{G}_A \cdot \mathbf{G}^B = \delta_A^B, \quad (19a)$$

$$\mathbf{g}_a \cdot \mathbf{g}^b = \delta_a^b, \quad (19b)$$

where δ_a^b is the Kronecker delta. The deformation gradient in the curvilinear coordinates is defined as

$$\mathbf{F} = \frac{\partial \mathbf{z}}{\partial \mathbf{Z}} = \frac{\partial \mathbf{z}}{\partial \boldsymbol{\xi}^i} \frac{\partial \boldsymbol{\xi}^i}{\partial \mathbf{Z}} = \frac{\partial \mathbf{z}}{\partial \boldsymbol{\xi}^i} \otimes \mathbf{G}^i = \mathbf{g}_i \otimes \mathbf{G}^i. \quad (20)$$

In the spirit of the solid shell formulation, any physical equation is expressed in the current curvilinear shell coordinate system. Thus, the coefficients of the right Cauchy-Green deformation tensor or Green's deformation tensor are expressed as

$$C_B^A = g_{ab} G^{AC} F_C^b F_B^a. \quad (21)$$

Meanwhile, the Green-Lagrange strain tensor is calculated as

$$E_B^A = \frac{1}{2}(C_B^A - \delta_B^A). \quad (22)$$

For simplicity, the St.Venant-Kirchhoff material is employed and, as a consequence, the second Piola-Kirchhoff stress tensor which relates forces in the reference configuration with areas in the reference configuration is defined as

$$S_B^A = \frac{1}{2} \lambda E_B^A + \mu E_B^A E_B^A. \quad (23)$$

On the other hand, the first Piola-Kirchhoff given which relates forces in the current configuration with areas in the reference configuration is given by

$$P_a^A = g_{ac} G^{AC} F_B^c S_C^B, \quad (24)$$

where P_a^A are the coefficients of stress tensor in current local and reference local coordinate systems. Alternately, the first Piola-Kirchhoff stress can be defined in global coordinate system as

$$P_i^I = G_{AI}^I g_i^a P_a^A. \quad (25)$$

At this point it is worth noting that by using the proposed prism elements to discretise shells, the thickness of the shell is not constant during deformation (i.e. in the current configuration) and the through-thickness stretching effect is captured. Therefore, the kinematics of the solid shell element is more comprehensive than the kinematics assumed in the Kirchhoff-Love theory.

4. Geometry and displacement approximations

4.1. Geometry approximation in the reference configuration

In order to maintain the practicality of the approach, a surface mesh which represents the mid-surface of the shell is first generated using a mesh generator. If the mid-surface is non-planar, higher order triangle elements could be used to better represent its geometry using the hierarchical shape functions described in Section 2. Having the mid-surface approximated, the geometry of a shell structure will be fully represented by only adding its thickness. The following describes the approximation of the necessary components of a shell's kinematics in the reference configuration.

First, the reference position of an arbitrary point on the shell's mid-surface in the global Cartesian coordinate system is calculated on a triangular mesh as follow

$${}^M Z_r(\xi, \eta) = \sum_v \phi^v(\xi, \eta) \underline{Z}_r^v + \sum_{e_t} \sum_\ell \phi_\ell^{e_t}(\xi, \eta) (\underline{Z}_r)_\ell^{e_t} + \sum_{\ell, m} \phi_{\ell m}^t(\xi, \eta) (\underline{Z}_r)_{\ell m}^t, \quad (26)$$

where \underline{Z} and the associated superscripts represent DOFs on vertex (v), edge (e_t), and triangle (t). Meanwhile, the right subscript $(\cdot)_r$ indicates coefficients of position vector in the global coordinate system. ϕ represents the shape functions associated with the DOFs on vertices, edges and triangles. The expression in Eq. (26) can be written in a vector-matrix form as follow

$${}^M \mathbf{Z}(\xi, \eta) = {}^3 \phi^v(\xi, \eta) \underline{\mathbf{Z}}^v + {}^3 \phi^{e_t}(\xi, \eta) \underline{\mathbf{Z}}^{e_t} + {}^3 \phi^t(\xi, \eta) \underline{\mathbf{Z}}^t = \sum_{g=v, e_t, t} {}^3 \phi^g(\xi, \eta) \underline{\mathbf{Z}}^g, \quad (27)$$

where the left superscript ${}^3(\cdot)$ indicates the matrix of shape functions for a three-component vector field.

Second, the through-thickness direction vector, of unit length, of a point on the mid-surface is approximated as follow

$${}^M \mathbf{D}(\xi, \eta) = \sum_{g=v, e_t, t} {}^3 \phi^g(\xi, \eta) \underline{\mathbf{D}}^g. \quad (28)$$

Third, the shell's thickness at a point on the mid-surface is calculated as follow

$${}^M a(\xi, \eta) = \sum_{g=v,e,t} {}^1 \phi^g(\xi, \eta) \underline{\mathbf{a}}^g, \quad (29)$$

where the left superscript ${}^1(\cdot)$ denotes the matrix of shape functions for a scalar field.

Finally, having all the necessary fields described and approximated, the reference position in the global Cartesian coordinate system of a point in a prism element is given by

$$\mathbf{Z}(\xi, \eta, \zeta) = {}^M \mathbf{Z}(\xi, \eta) + {}^M a(\xi, \eta) \left(\zeta - \frac{1}{2} \right) {}^M \mathbf{D}(\xi, \eta). \quad (30)$$

Similarly, it can be expressed in a compact form as follow

$$\mathbf{Z}(\xi, \eta, \zeta) = \sum_{s=L,U} \sum_{g=v,e,t} {}^3 \phi_s^g(\xi, \eta, \zeta) \underline{\mathbf{Z}}_s^g. \quad (31)$$

Next, the Jacobian is derived to transform a point from a prism element's local coordinate system to the global Cartesian coordinate system. In order to keep the derivation straightforward, the thickness of the shell is assumed constant, i.e. ${}^M a(\xi, \eta) = \text{const} = a$. Using Eq. (30), the Jacobian is then defined as follow

$$\mathbf{J}(\xi, \eta, \zeta) = \frac{\partial \mathbf{Z}}{\partial \boldsymbol{\xi}} = {}^M \mathbf{J}(\xi, \eta) + {}^D \mathbf{J}(\xi, \eta, \zeta), \quad (32)$$

where the first term contributed by the mid-surface components is

$${}^M \mathbf{J}(\xi, \eta, \zeta) = \begin{bmatrix} \frac{\partial_0^M Z}{\partial \xi} & \frac{\partial_0^M Z}{\partial \eta} & 0 \\ \frac{\partial_1^M Z}{\partial \xi} & \frac{\partial_1^M Z}{\partial \eta} & 0 \\ 0 & 0 & 0 \end{bmatrix}, \quad (33)$$

and the second term contributed by the through-thickness component is

$${}^D \mathbf{J}(\xi, \eta, \zeta) = a \begin{bmatrix} 0 & 0 & \frac{M}{0} D \\ 0 & 0 & \frac{M}{1} D \\ 0 & 0 & \frac{M}{2} D \end{bmatrix} + a \left(\zeta - \frac{1}{2} \right) \begin{bmatrix} \frac{\partial_0^M D}{\partial \xi} & \frac{\partial_0^M D}{\partial \eta} & 0 \\ \frac{\partial_1^M D}{\partial \xi} & \frac{\partial_1^M D}{\partial \eta} & 0 \\ \frac{\partial_2^M D}{\partial \xi} & \frac{\partial_2^M D}{\partial \eta} & 0 \end{bmatrix}. \quad (34)$$

4.2. Curvilinear systems in reference and current configuration

A local curvilinear basis in the reference configuration, with basis vectors \mathbf{G}_α , is established. The in-plane components of \mathbf{G}_α are approximated using hierarchical approximation functions as follows

$${}^M \mathbf{G}_0(\xi, \eta) = G_I^0 \mathbf{I}^I = \left\{ \sum_{g=v,e,t} {}^3 \phi^g(\xi, \eta) \underline{\mathbf{G}}_0^g \right\} \mathbf{I}^I, \quad (35a)$$

$${}^M \mathbf{G}_1(\xi, \eta) = G_I^1 \mathbf{I}^I = \left\{ \sum_{g=v,e,t} {}^3 \phi^g(\xi, \eta) \underline{\mathbf{G}}_1^g \right\} \mathbf{I}^I, \quad (35b)$$

where \mathbf{I} is the global Cartesian basis vector, as shown in Fig. 2. Meanwhile, the local basis vector in the through-thickness direction is given by

$${}^M\mathbf{G}_2(\xi, \eta) = G_I^2 \mathbf{I}^I = \{\text{Spin}[^M\mathbf{G}_0(\xi, \eta)]^M\mathbf{G}_1(\xi, \eta)\} \mathbf{I}^I, \quad (36)$$

where $\text{Spin}[\cdot]$ is the spin operator acting as a vector product. In particular, for an axis a_i , the spin tensor is defined as

$$\text{Spin}[\mathbf{a}] = \begin{bmatrix} 0 & -a_3 & a_2 \\ a_3 & 0 & -a_1 \\ -a_2 & a_1 & 0 \end{bmatrix}, \quad (37)$$

and the cross product of \mathbf{a} and an arbitrary vector \mathbf{b} is expressed as

$$\mathbf{a} \times \mathbf{b} = \text{Spin}[\mathbf{a}]\mathbf{b} = -\text{Spin}[\mathbf{b}]\mathbf{a} = -\mathbf{b} \times \mathbf{a}. \quad (38)$$

The local curvilinear basis vectors \mathbf{G}_0 , \mathbf{G}_1 , and \mathbf{G}_2 are visualised in Fig. 3.

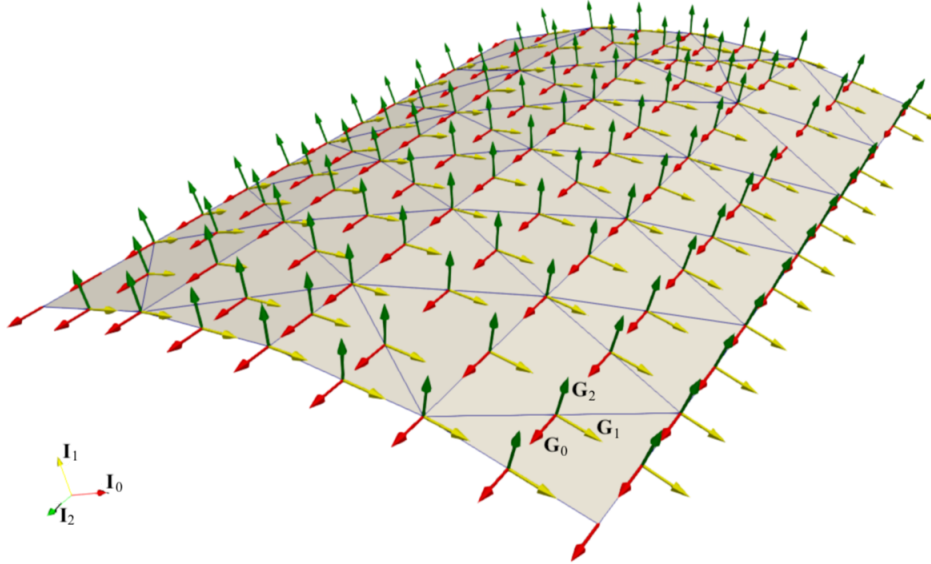


Figure 3: Approximated local curvilinear basis vector \mathbf{G}_0 (red), \mathbf{G}_1 (yellow), and \mathbf{G}_2 (green) on the mesh of a curved shell.

The local curvilinear coordinate basis in the current configuration, which is convected by shell mid-surface motion, is given as

$$\mathbf{g}_a = g_a^i \mathbf{i}_i = {}^M F_I^i {}^M G^{AI} \delta_A^a \mathbf{i}_i, \quad (39)$$

where ${}^M F_I^i(\xi, \eta, \zeta)$ are local components of the deformation gradient. It should be noted that, for a discretised system, the deformation gradient is additively decomposed into a part resulting from through-thickness DOFs and a part from the upper and lower triangles' DOFs. Basis vector \mathbf{i}_i is a Cartesian basis vector for the current configuration, which could be set independently from the Cartesian basis \mathbf{I}_i . However, for the rest of paper, we restrict ourself to the case where $\mathbf{i}_i \equiv \mathbf{I}_i$. This can be considered a generalisation of the co-rotational formulation for shells.

4.3. Displacement approximations

The position of a material point in the current configuration is given by

$$z^J \mathbf{I}_J = Z^J \mathbf{I}_J + u^J \mathbf{I}_J + v g_2^J \mathbf{I}_J + w^\alpha g_\alpha^J \mathbf{I}_J, \quad (40)$$

where the displacement coefficients u^J are DOFs associated with the vertices, edges and faces of the upper and lower triangles, and expressed in the global Cartesian coordinate system. The displacement coefficients v and w^α are DOFs associated with the edges and faces of the quadrilaterals through the shell thickness, and expressed in terms of the current curvilinear (convected) coordinate system. These displacement DOFs are illustrated in Fig. 4.

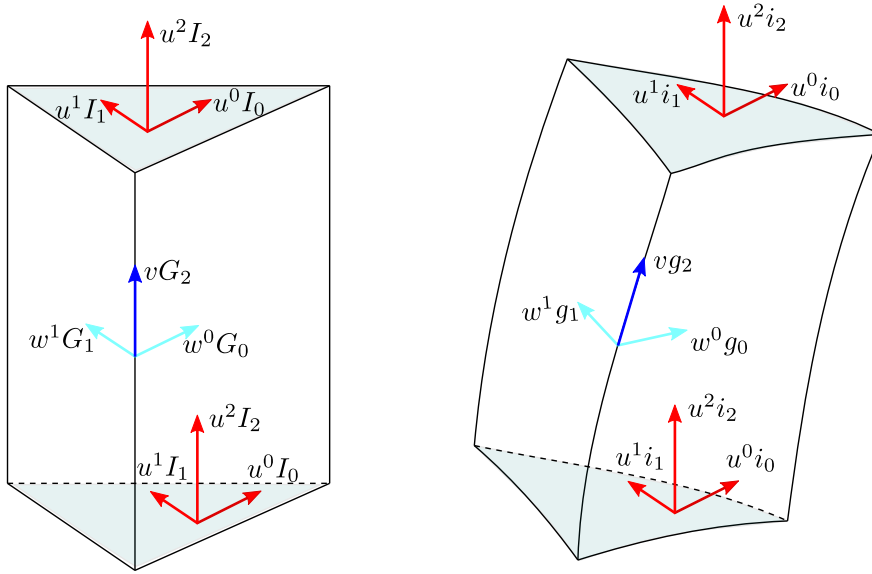


Figure 4: Displacement components \mathbf{u} , \mathbf{v} , and \mathbf{w} and their associated bases (global Cartesian bases \mathbf{I} , \mathbf{i} and local convected curvilinear bases \mathbf{G} , \mathbf{g}) in the reference (left) and current (right) configurations.

The displacement vector \mathbf{u} on the top and bottom triangles is approximated as follow

$$\mathbf{u}(\boldsymbol{\xi}) = \sum_{s=L,U} \sum_{g=v,e,t} {}^3\phi_s^g(\boldsymbol{\xi}) \underline{\mathbf{u}}_s^g = [{}^3\bar{\boldsymbol{\phi}}(\boldsymbol{\xi})] \underline{\mathbf{u}}, \quad (41)$$

with the displacement DOFs in vector $\underline{\mathbf{u}}$ expressed in the global Cartesian coordinate system. This allows elements to be assembled with other tetrahedral elements without the need for any linking or transfer elements. Meanwhile, the through-thickness displacements $\mathbf{v} = v g_2^J \mathbf{I}_J$ and $\mathbf{w} = w^\alpha g_\alpha^J \mathbf{I}_J$ are approximated in the local curvilinear system which follows the global mid-surface deformation. The coefficients v and w^α are given by

$$v(\boldsymbol{\xi}) = \sum_{g=e,q,p} {}^1\phi^g(\boldsymbol{\xi}) \underline{\mathbf{v}}^g = [{}^1\bar{\boldsymbol{\phi}}(\boldsymbol{\xi})] \underline{\mathbf{v}}, \quad (42a)$$

$$\mathbf{w}(\boldsymbol{\xi}) = \sum_{g=e,q,p} {}^2\phi^g(\boldsymbol{\xi}) \underline{\mathbf{w}}^g = [{}^2\bar{\boldsymbol{\phi}}(\boldsymbol{\xi})] \underline{\mathbf{w}}. \quad (42b)$$

Having \mathbf{u} , \mathbf{v} and \mathbf{w} derived, the gradient of displacements can be calculated as follows

$$\nabla_{Z^J} u^i (\mathbf{I}_i \otimes \mathbf{I}^J) = \left\{ \sum_{s=U,L} \sum_{g=v,e,t} \frac{\partial^3 \{\phi_s^g\}^i \mathbf{I}_i}{\partial \xi^k} J_J^k \right\} \underline{\mathbf{u}}_s^g \otimes \mathbf{I}^J, \quad (43a)$$

$$\nabla_{X^A} u^a = g_j^a \nabla_{Z^J} w^j G_A^J, \quad (43b)$$

and the gradients of higher-order through thickness displacements

$$\nabla_{X^A} v^a (\mathbf{g}_a \otimes \mathbf{G}^A) = \left\{ \sum_{g=e,q,p} \frac{\partial^1 \{\phi^g\}^a \mathbf{g}_a}{\partial \xi^k} J_J^k G_A^J \right\} \underline{\mathbf{v}}^g \otimes \mathbf{G}^A, \quad (44a)$$

$$\nabla_{X^A} w^a (\mathbf{g}_a \otimes \mathbf{G}^A) = \left\{ \sum_{g=e,q,p} \frac{\partial^2 \{\phi^g\}^a \mathbf{g}_a}{\partial \xi^k} J_J^k G_A^J \right\} \underline{\mathbf{w}}^g \otimes \mathbf{G}^A. \quad (44b)$$

Consequently, the deformation gradient is calculated as

$${}^M F_I^i = \delta_I^i + \nabla_{Z^I} u^i = \delta_I^i + [\nabla_{Z^I} \phi^i(\boldsymbol{\xi})] \underline{\mathbf{u}}, \quad (45a)$$

$$F_A^a = g_i^a G_A^I \delta_I^i + \nabla_{X^A} v^a + \nabla_{X^A} w^a = g_i^a G_A^I \delta_I^i + [\nabla_{X^A} \phi(\boldsymbol{\xi})] \underline{\mathbf{v}} + [\nabla_{X^A} \phi(\boldsymbol{\xi})] \underline{\mathbf{w}}. \quad (45b)$$

It will be shown later in Section 5 that the approximation order for the in-plane displacements through the thickness of the shell should be at least second-order to avoid locking. It should be noted that when only DOFs are set on triangle entities, the approximation of displacement through the thickness is linear. The DOFs associated with the quadrilaterals' edges and faces, and prism volume are higher orders and defined in curvilinear coordinate system which is convected by the deformation gradient ${}^M \mathbf{F}$.

4.4. Element formulation

With all the physical quantities derived and approximated, the vector of internal forces for the top/bottom surfaces and through-thickness direction are respectively expressed as follows

$$\mathbf{f}_u^{\text{int}}(\underline{\mathbf{u}}, \underline{\mathbf{v}}, \underline{\mathbf{w}}) = \int_{\Omega} [\nabla_{Z^I} \phi^I] P_i^I(\underline{\mathbf{u}}, \underline{\mathbf{v}}, \underline{\mathbf{w}}) d\Omega, \quad (46a)$$

$$\mathbf{f}_v^{\text{int}}(\underline{\mathbf{u}}, \underline{\mathbf{v}}, \underline{\mathbf{w}}) = \int_{\Omega} [\nabla_{X^A} \phi^A] P_a^A(\underline{\mathbf{u}}, \underline{\mathbf{v}}, \underline{\mathbf{w}}) d\Omega, \quad (46b)$$

$$\mathbf{f}_w^{\text{int}}(\underline{\mathbf{u}}, \underline{\mathbf{v}}, \underline{\mathbf{w}}) = \int_{\Omega} [\nabla_{X^A} \phi^A] P_a^A(\underline{\mathbf{u}}, \underline{\mathbf{v}}, \underline{\mathbf{w}}) d\Omega, \quad (46c)$$

where Ω is the domain occupied by the shell.

The nonlinear problem is solved using the Newton-Raphson method in which a Taylor series expansion of the residual vector is truncated after the linear term:

$$\begin{bmatrix} \frac{\partial \mathbf{f}_u^{\text{int}}(\underline{\mathbf{u}}, \underline{\mathbf{v}}, \underline{\mathbf{w}})}{\partial \underline{\mathbf{u}}} & \frac{\partial \mathbf{f}_u^{\text{int}}(\underline{\mathbf{u}}, \underline{\mathbf{v}}, \underline{\mathbf{w}})}{\partial \underline{\mathbf{v}}} & \frac{\partial \mathbf{f}_u^{\text{int}}(\underline{\mathbf{u}}, \underline{\mathbf{v}}, \underline{\mathbf{w}})}{\partial \underline{\mathbf{w}}} \\ \frac{\partial \mathbf{f}_v^{\text{int}}(\underline{\mathbf{u}}, \underline{\mathbf{v}}, \underline{\mathbf{w}})}{\partial \underline{\mathbf{u}}} & \frac{\partial \mathbf{f}_v^{\text{int}}(\underline{\mathbf{u}}, \underline{\mathbf{v}}, \underline{\mathbf{w}})}{\partial \underline{\mathbf{v}}} & \frac{\partial \mathbf{f}_v^{\text{int}}(\underline{\mathbf{u}}, \underline{\mathbf{v}}, \underline{\mathbf{w}})}{\partial \underline{\mathbf{w}}} \\ \frac{\partial \mathbf{f}_w^{\text{int}}(\underline{\mathbf{u}}, \underline{\mathbf{v}}, \underline{\mathbf{w}})}{\partial \underline{\mathbf{u}}} & \frac{\partial \mathbf{f}_w^{\text{int}}(\underline{\mathbf{u}}, \underline{\mathbf{v}}, \underline{\mathbf{w}})}{\partial \underline{\mathbf{v}}} & \frac{\partial \mathbf{f}_w^{\text{int}}(\underline{\mathbf{u}}, \underline{\mathbf{v}}, \underline{\mathbf{w}})}{\partial \underline{\mathbf{w}}} \end{bmatrix} \begin{Bmatrix} \delta \underline{\mathbf{u}} \\ \delta \underline{\mathbf{v}} \\ \delta \underline{\mathbf{w}} \end{Bmatrix} = \begin{bmatrix} \mathbf{f}_u^{\text{ext}} - \mathbf{f}_u^{\text{int}}(\underline{\mathbf{u}}, \underline{\mathbf{v}}, \underline{\mathbf{w}}) \\ -\mathbf{f}_v^{\text{int}}(\underline{\mathbf{u}}, \underline{\mathbf{v}}, \underline{\mathbf{w}}) \\ -\mathbf{f}_w^{\text{int}}(\underline{\mathbf{u}}, \underline{\mathbf{v}}, \underline{\mathbf{w}}) \end{bmatrix}, \quad (47)$$

where $\delta \mathbf{u}$, $\delta \mathbf{v}$ and $\delta \mathbf{w}$ are the iterative changes in displacements in the global and current local coordinate systems, and the left hand matrix represent the tangent matrix. Additionally, since the solution is strongly nonlinear and potentially includes local instabilities, the classical quadratic arc-length method with line search is employed.

As can be seen in Eq. (47), the external forces are applied only to the DOFs associated with the upper and lower triangles, which are expressed in the global Cartesian coordinate system. Meanwhile, all DOFs associated with the convected curvilinear system are internal and there is no external forces act on them, except body forces.

It is worth noting that in this proposed formulation, the current curvilinear system follows the shell deformation described by DOFs on the upper and lower triangle. This is similar to the co-rotational formulation presented by Crisfield [21] in which the coordinate system is rotated while the shell is deforming and the tangent stiffness is non-symmetric. However, for the present problem, numerical experiments show that the tangent stiffness matrix becomes symmetric as the iterative procedure reaches equilibrium state. Therefore, the matrix can be symmetrised without deteriorating the convergence order.

5. Numerical examples

Table 5: Geometry, material, and loading data

Parameter	Linear analysis [†]		Nonlinear analysis [‡]			
	PC-L	SLR	SAP	HS	POC	PC
<i>Geometry</i>						
Length, L	600	50	N/A	N/A	10.35	200
Radii, $R/R_i/R_o$	300	25	6/10	10	4.953	100
Thickness, a	3	0.25	0.03	0.04	0.094	1
Angle, θ	N/A	40 ^o	N/A	18 ^o	N/A	N/A
<i>Material</i>						
Young's modulus, E	3	4.32 $\times 10^8$	21 $\times 10^6$	6.825 $\times 10^7$	10.5 $\times 10^6$	30 $\times 10^3$
Poisson's ratio, ν	0.3	0.0	0.0	0.3	0.3125	0.3
<i>Loading</i>						
Point force, P	1	N/A	N/A	400	40,000	12,000
Distributed force, q	N/A	90	0.8	N/A	N/A	N/A

[†]PC-L - Pinched cylinder for linear analysis; SLR - Scordelis-Lo Roof

[‡] SAP - Slit annular plate; HS - Hemispherical shell; POC - Pullout cylinder; PC - Pinched cylinder

5.1. Linear analysis

5.1.1. Pinched cylinder

A linear analysis of a cylinder mounted on a diaphragm, subject to pinching forces, is presented to demonstrate the accuracy of the proposed approach as well as its capability

to avoid locking effects. The input data can be found in Table 5. Only one eighth of the geometry is discretised due to symmetry. As can be seen in Fig. 5, both meshes (coarse and fine) yield good convergence results compared to those reported in the literature [22]. For both meshes, there are clear signs of locking when only linear polynomials are employed for the through-thickness approximation of the in-plane displacement, \mathbf{w} . However, when this is increased to second order, the locking phenomenon is alleviated for both meshes.

Fig. 5 shows convergence plots for both the coarse and fine meshes as the order of approximation for the triangular faces of the prism elements are increased from first to eighth order. It can also be observed that only increasing the through-thickness order of approximation for the displacement in the through-thickness direction v has minimal effects on the results. Therefore, second-order approximations will also be applied for v for the rest of the examples presented in this paper, unless otherwise stated. It should be noted that for visualisation purposes and because of the linear nature of the problem, the deformed shape in Fig. 5 is presented as if the cylinder is subject to pullout forces rather than pinched, as shown in the literature. Since the small displacement assumption is made in this example for comparison purpose, the direction of the load, inward or outward, does not change the character of the results.

5.1.2. Scordelis-Lo Roof

In this example, analysis of the well-known Scordelis-Lo Roof is considered in order to demonstrate both the performance of the prism element and how the properties of the heterogeneous and hierarchical shape functions can be utilised to build an efficient multi-grid solver.

Fig. 6 shows the configuration of the roof which is clamped at two ends and free along the other edges. The input geometry and material parameters are provided in Table 5. The roof is subjected to a uniformly distributed self-weight load of $q = 90$ per unit area. Due to symmetry, only one quadrant of the full roof is considered for analysis as shown in Fig. 6.

As validation, a linear analysis of the roof was undertaken and the vertical displacement at point A (middle of the free edge as shown in Fig. 6) is observed and compared to a reference value provided by Belytschko et al. [22]. By employing elements with anisotropic shape functions, in which fifth order is used for the approximation functions on the upper and lower faces and second-order through the thickness, the vertical displacement at point A is calculated as 0.3176. This is slightly softer but comparable to the reference results of 0.3024 [22] in which a 9-node element with uniform 2×2 quadrature and γ -stabilisation was used. The deformed shape and vertical displacement of the full structure of Scordelis-Lo Roof is given in Fig. 7.

Fig. 8 shows the convergence of the analyses for Scordelis-Lo Roof with coarse, middle, and fine meshes for increasing order of approximation on the upper and lower faces. As can be seen, all three cases yield an exponential rate of convergence. The slight increase in error for the fine mesh for a very large number of DOFs can be attributed to the tolerance of the linear solver, matrix conditioning, and the floating precision of the machine as the approximation error becomes small.

The efficiency of the proposed prism elements based on hierarchical shape functions is

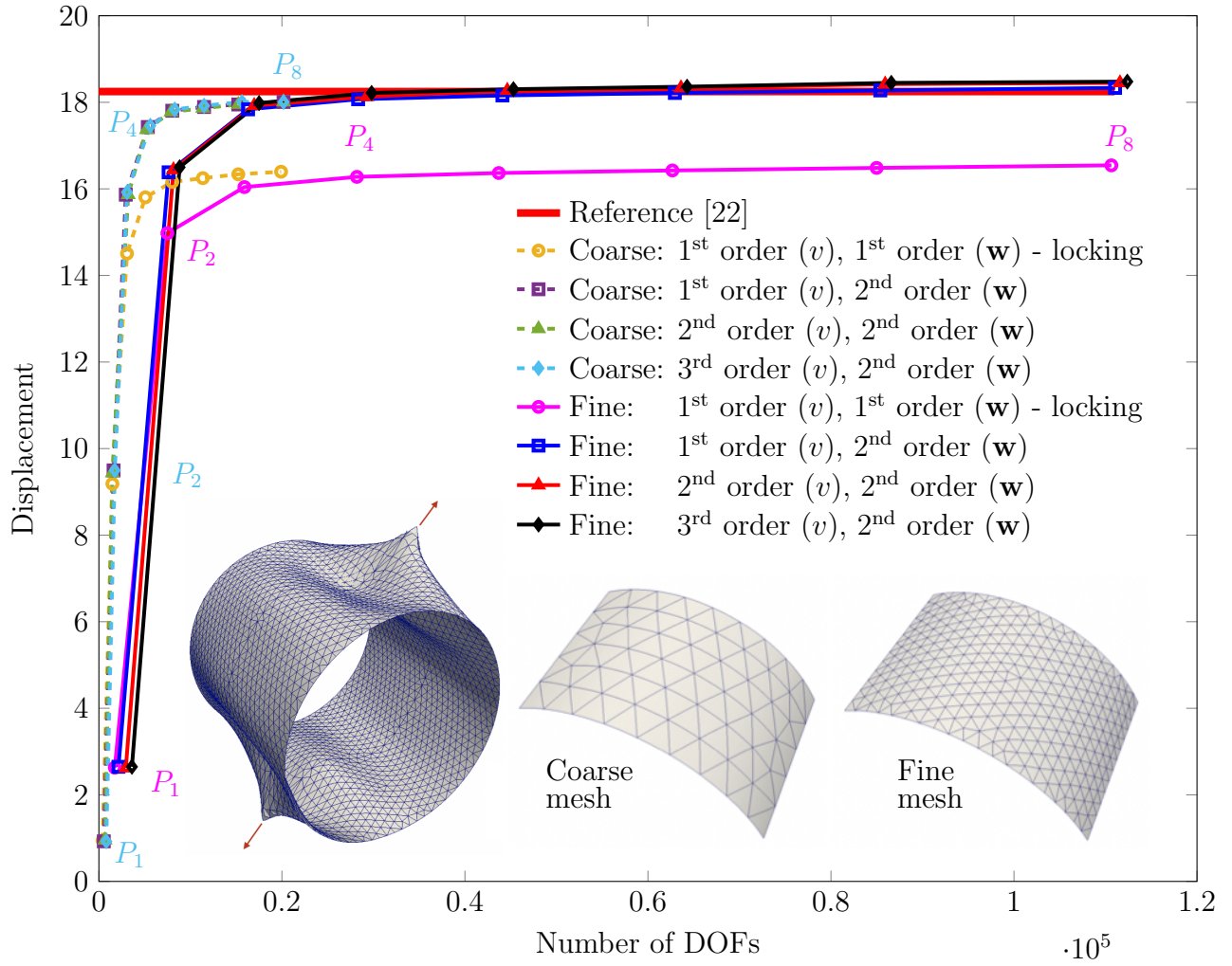


Figure 5: Convergence of displacement with different meshes and polynomial orders. P_n indicates result using n^{th} order polynomial for displacement component \mathbf{u} (applies to all lines).

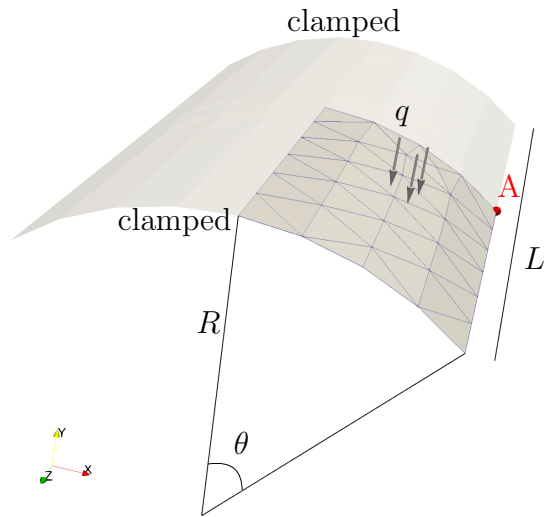


Figure 6: Scordelis-Lo roof geometry, boundary conditions and loading.

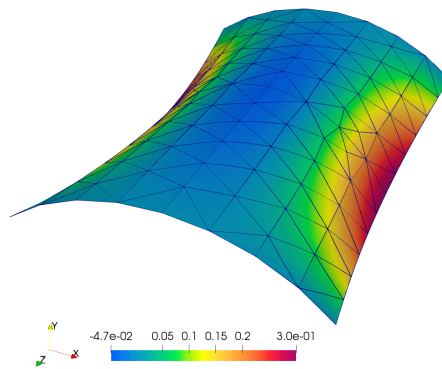


Figure 7: Deformation of Scordelis-Lo roof with fifth-order approximations for the upper and lower faces. Contours of vertical displacement.

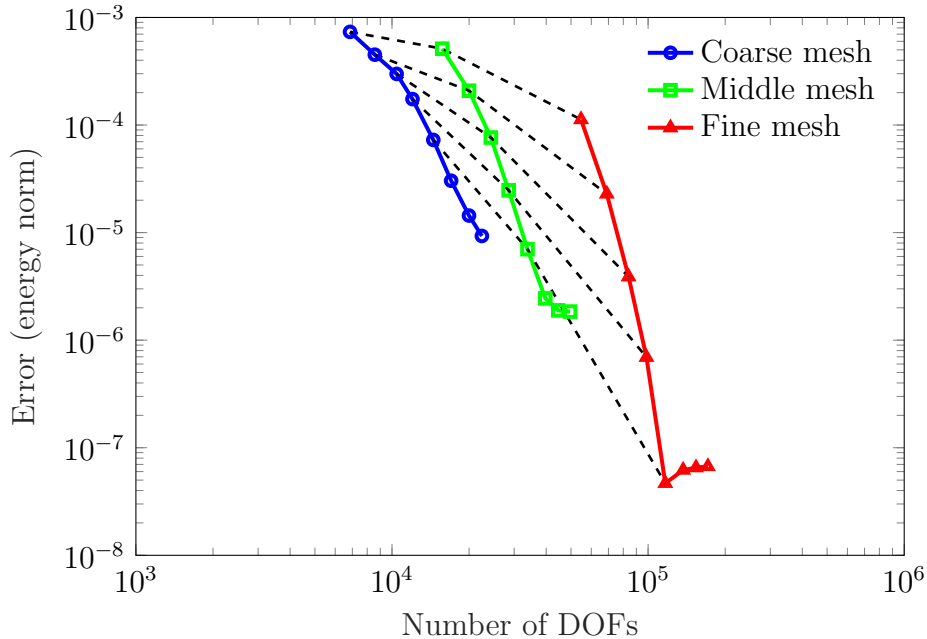


Figure 8: Exponential convergence of Scordelis-Lo roof problem with three different meshes. Solid lines represent errors generated from different polynomial orders (first to eighth) of the same mesh. Dashed lines represent errors from different meshes with the same polynomial order (from first to fifth).

demonstrated using a more complex geometry of the Scordelis-Lo Roof, with perforations. Fig. 9 shows this modified geometry with uniformly distributed holes. Each hole has a radius of 0.3. Once again, due to symmetry, only a quarter of the perforated roof is considered. The perforated roof is initially analysed using second-order approximations on the triangular faces, yielding poor results, as expected. The error in energy norm is distributed non-uniformly across the roof with the largest errors observed near the outer edge of the structure as shown in Fig. 10. This *a posteriori* error estimator is subsequently employed to drive adaptivity, in which one third of the elements with the highest error are selected to locally increase the order of approximation. This creates a heterogeneous distribution of approximation, ranging from second to eighth-order. An iterative adaptive refinement process is undertaken, leading to a highly accurate result with low errors across the roof.

It is worth noting that, in this example of linear analysis, that a multigrid solver is utilised to significantly increase the speed of solving the system of equations. Due to its scalability, the multigrid solver, along with hierarchical shape functions and an error estimator, appears to be a highly effective combination in achieving an efficient analysis using multiple processors. Furthermore, the anisotropic and heterogeneous properties of the shape functions support more flexibility, leading to accurate results with minimum additional DOFs. Fig. 11 shows that the multigrid solver scales well with increasing numbers of processors. It also shows the excellent scalability of the assembly process.

For the unperforated roof, due to the relative simplicity of the problem and small number of DOFs, there is a sign of saturation. In contrast, a direct solver (SuperLU_DIST [23])

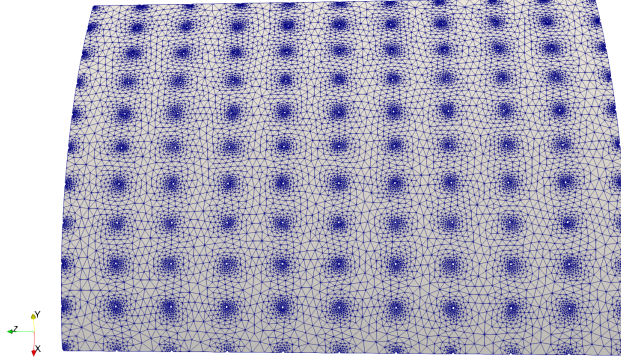


Figure 9: Mesh of a quarter of Scordelis-Lo roof with perforations.

performs slightly better for a small number of processors. However, its performance quickly deteriorates as the number of processors grow. This can be attributed to increased matrix fill-in when the problem is distributed over many processors. After a certain point, with more processors, the speed-up for the direct solver even decreases.

5.2. Geometrically nonlinear analysis

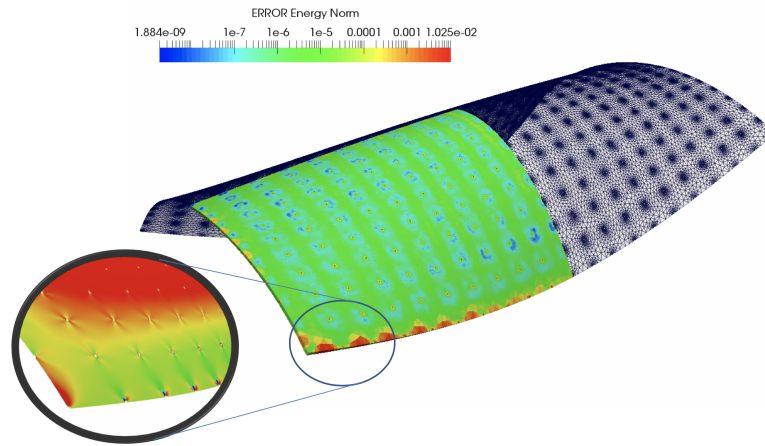
5.2.1. Slit annular plate

The nonlinear analysis of a slit annular plate, subject to an edge force, is considered as a standard benchmark for the nonlinear analysis shells. Fig. 12 shows the geometry and mesh for this problem. The input data is provided in Table 5. One side of the slit is fully clamped and the other side is subjected a uniformly distributed edge load which is kept vertical during the entire simulation. The vertical displacements of point A (red) and point B (blue) at two ends of the edge are observed and compared to those in the literature. Fig. 13 presents the displacements at both points for increasing force, comparing different order of approximation on the upper and lower faces. Once again, second-order approximations are adopted through the thickness of the element.

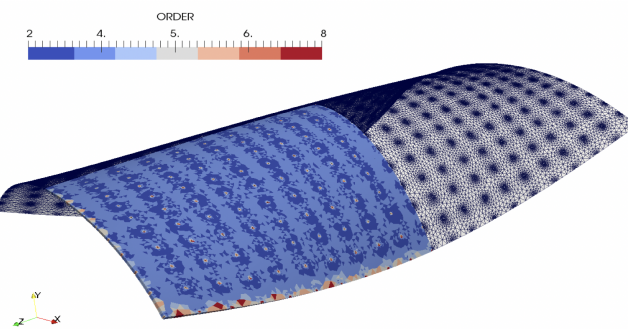
It can be observed that a second-order approximation on the top and bottom triangles yields substantially stiffer results compared to the results reported by Sze et al. [24]. This volume locking can be attributed to the coarse mesh and low order of approximation employed. However, as the approximation is raised to third and fourth orders, locking is alleviated and the vertical displacements at points A and B agree very well with the reference. The deformed shapes of the plate for third order approximation are shown in Fig. 14.

5.2.2. Hemispherical shell

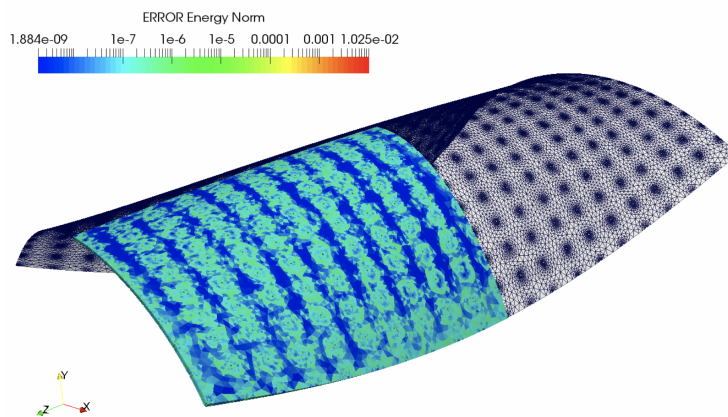
Fig. 15 shows the geometry and mesh configuration of a hemispherical shell with an 18° cutout at its pole. Detailed dimensions and material properties of the structure can be found in Table 5. Due to symmetry, only one quarter of the shell with symmetric boundary conditions is analysed. Vertical displacement is restricted along the bottom edge. The radial displacement at points A and B are observed and compared with the reference



(a) Error distribution before p -refinement



(b) Heterogeneous local p -refinement with colour bar showing polynomial orders



(c) Error distribution after p -refinement

Figure 10: Multigrid solver with *a posteriori* error estimator used for analysis of perforated Scordelis-Lo roof.

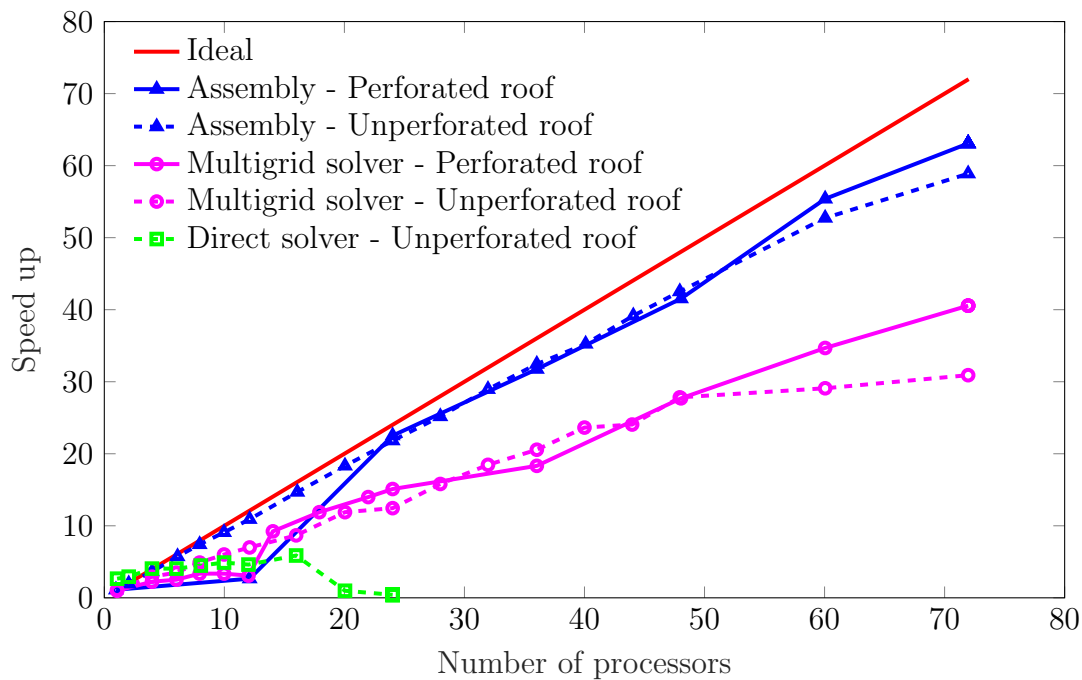


Figure 11: Speedup for assembly and solver for unperforated and perforated Scordelis-Lo roof.

[24]. This hemispherical shell problem is considered a valuable test challenging test due to the inextensional bending modes with almost no membrane strains. Further, since a large portion of the shell rotates under the given loads, it is also a useful test to evaluate the capability of the element in handling rigid body rotation about normals to the shell surfaces [22].

Similar to the previous example, a coarse mesh with only 100 elements is used to analyse the shell and evaluate the performance of the proposed approach, with second-order approximations through the thickness. The approximations constructed on the upper and lower

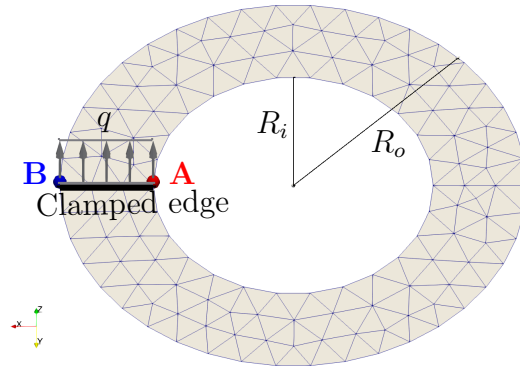


Figure 12: Configuration of slit annular plate.

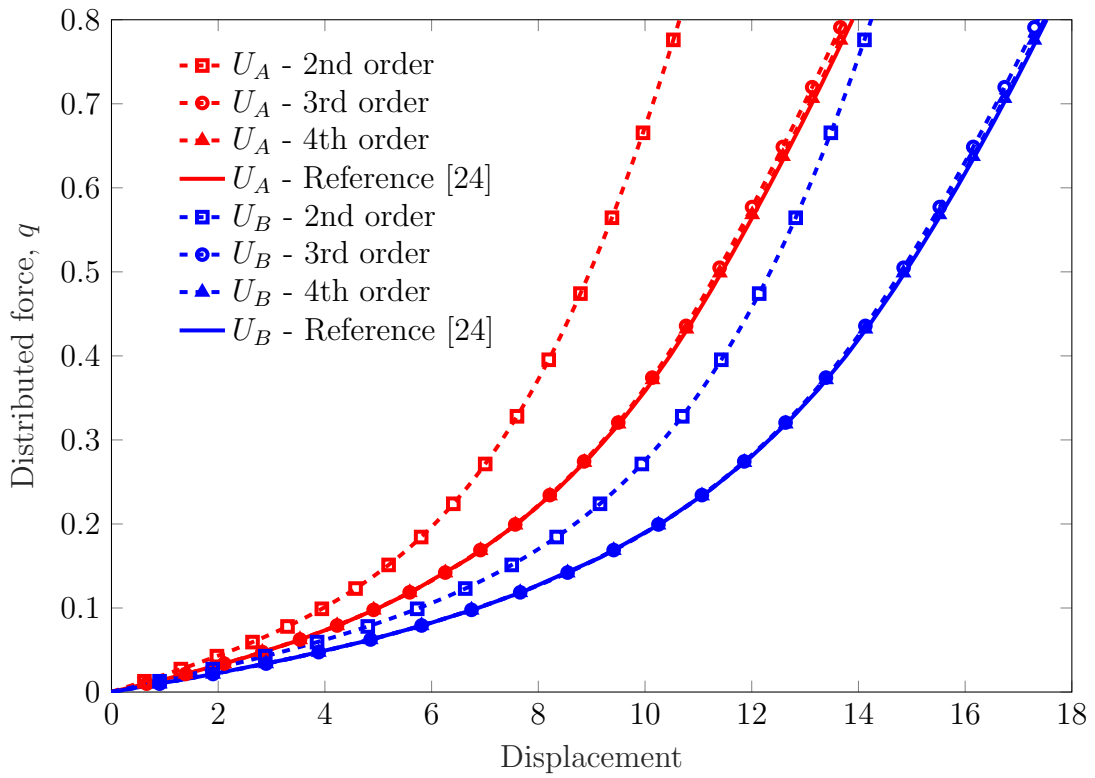


Figure 13: Comparison of slit annular plate at observed points with different orders of approximation for the upper and lower faces.

faces are varied from second to fifth orders. As in the previous problem, a lower order of approximation leads to volumetric locking and a stiff result, as shown in Fig. 16. However, the locking appears to be alleviated when fourth and fifth orders of approximation are employed and the results are in good agreement with those reported in the literature [24] for both points A and B. Fig. 17 presents the deformed shapes for third-order approximations.

5.2.3. *Cylindrical shell bearing pull-out forces*

Fig. 18 shows the geometry and mesh of an open-ended cylindrical shell subjected to a pair of radial forces P . Due to symmetry, only one eighth of the shell is analysed and the radial displacement of points A, B, and C are observed and compared to the reference [24]. The geometry and material data can be found in Table 5.

Due to the relatively fine mesh being used, the radial displacement of the observed points shows good agreement with those reported by Sze et al. [24], even with second or third orders of approximation on the prism upper and lower faces. This is illustrated in load-displacement plot in Fig 19.

The large and complex displacements of point C at the edge of the shell is captured well by the proposed approach. The deformed shapes at three analysis steps with third-order approximations are presented in Fig. 20. Second-order approximations were adopted in the through-thickness direction for all analyses.

5.2.4. *Pinched cylindrical shell*

This example is similar to the previous but the cylindrical shell is mounted on to rigid diaphragms at each end, restricting in-plane displacements. The geometry and mesh configuration and its details are presented in Fig. 21 and Table 5, respectively. Once again, due to symmetry, one eighth of the cylinder is analysed. This test is particularly challenging due to the need to capture both the inextensional bending modes and the complex membrane states which the cylinder exhibits during deformation [22].

Fig. 22 presents the displacements at observed points A and B of the shell in comparison with the reference [24]. Similar to the previous examples, second order approximation is employed in the through-thickness direction and various orders are investigated for upper and lower faces. As can be seen, there is good agreement with the reference results. Meanwhile, the shapes of the pinched shell at three stages of the analysis are shown in Fig. 23, where the large and complex deformation at the middle of the cylinder (point B) is captured. The analysis ends when the two sides of the cylinder meet.

6. Concluding remarks

In this study, the formulation of a prism element using shape functions that are hierarchical, heterogeneous, and anisotropic is presented for solving complex nonlinear behaviour of solve solid shell problems. Unlike classical degenerated shell theory, the solid shell theory requires only displacement DOFs, enabling them to be combined with classical solid elements if required and avoids complex description of boundary conditions. Furthermore, stretching

in the through-thickness direction is captured and general 3D constitutive equations can be used without simplification or modification.

Additionally, element of this type enables modelling of coupled multi-physics problems as well as utilisation of more sophisticated hyperelastic models since the material is defined in a standard 3D setting.

The hierarchical properties of the shape functions enable an efficient iterative solver to be employed, that is tailored for *hp*-adaptive implementation. The heterogeneous property of the shape functions enables the use of arbitrary orders of approximation that can be set independently for each mesh entity, i.e. edge, triangle, quadrilateral, and prism. The anisotropic property permits the approximation functions on the upper and lower faces to be defined independently from approximation through the thickness of the element. Thus, locking problems, that are common in solid shell formulations, are alleviated simply by increasing the order of approximation, without resorting to enhancements, such as reduced integration or additional assumed natural strain or enhanced strain fields.

Looking forward, through layering of the the proposed prism elements can be easily applied for modelling laminated structures and the delamination is captured by adding standard cohesive/interface elements between layers. It is also straightforward to add dissipative processes such as plasticity or fracture.

The formulation has been implemented in the MoFEM library [1]. Both the code and the data for the numerical examples are open-source [2].

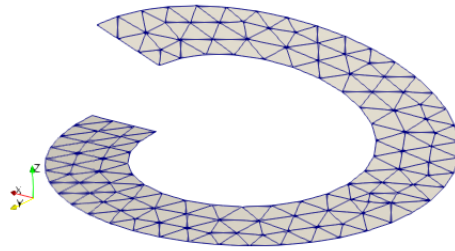
Acknowledgements

The authors gratefully acknowledge the support provided by the EPSRC Strategic Support Package: Engineering of Active Materials by Multiscale/Multiphysics Computational Mechanics - EP/R008531/1.

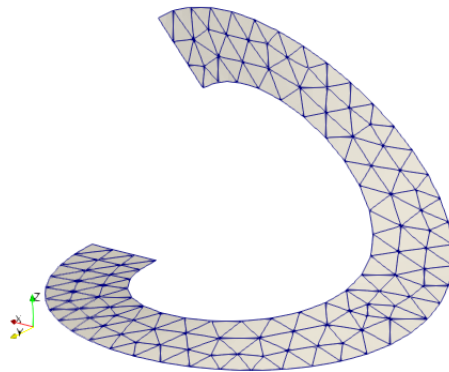
References

- [1] L. Kaczmarczyk, Z. Ullah, K. Lewandowski, X. Meng, X.-Y. Zhou, I. Athanasiadis, H. Nguyen, C.-A. Chalons-Mouriesse, E. Richardson, E. Miur, A. Shvarts, M. Wakeni, C. Pearce, MoFEM: An open source, parallel finite element library, *Journal of Open Source Software* 5 (45) (2020) 1441. doi:10.21105/joss.01441.
- [2] A. Author, B. Author, Supplement source code and data for solid shell analyses (to be appeared), Zenodo (2020). doi:10.xxxx/zenodo.xxxxx.
- [3] H. Parisch, A continuum-based shell theory for non-linear applications, *International Journal for Numerical Methods in Engineering* 38 (11) (1995) 1855–1883. doi:10.1002/nme.1620381105.
- [4] R. Hauptmann, K. Schweizerhof, A systematic development of ‘solid-shell’ element formulations for linear and non-linear analyses employing only displacement degrees of freedom, *International Journal for Numerical Methods in Engineering* 42 (1) (1998) 49–69. doi:10.1002/(SICI)1097-0207(19980515)42:1<49::AID-NME349>3.0.CO;2-2.
- [5] S. Hosseini, J. J. C. Remmers, C. V. Verhoosel, R. d. Borst, An isogeometric solid-like shell element for nonlinear analysis, *International Journal for Numerical Methods in Engineering* 95 (3) (2013) 238–256. doi:10.1002/nme.4505.
- [6] L. Leonetti, F. Liguori, D. Magisano, G. Garcea, An efficient isogeometric solid-shell formulation for geometrically nonlinear analysis of elastic shells, *Computer Methods in Applied Mechanics and Engineering* 331 (2018) 159–183. doi:10.1016/j.cma.2017.11.025.

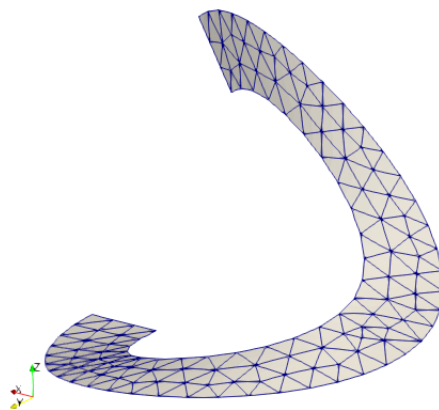
- [7] F. Hashagen, R. de Borst, Numerical assessment of delamination in fibre metal laminates, *Computer Methods in Applied Mechanics and Engineering* 185 (2) (2000) 141–159. doi:10.1016/S0045-7825(99)00256-X.
- [8] J. J. C. Remmers, G. N. Wells, R. d. Borst, A solid-like shell element allowing for arbitrary delaminations, *International Journal for Numerical Methods in Engineering* 58 (13) (2003) 2013–2040. doi:10.1002/nme.907.
- [9] L. Vu-Quoc, X. G. Tan, Optimal solid shells for non-linear analyses of multilayer composites. I. Statics, *Computer Methods in Applied Mechanics and Engineering* 192 (9) (2003) 975–1016. doi:10.1016/S0045-7825(02)00435-8.
- [10] L. Vu-Quoc, X. G. Tan, Optimal solid shells for non-linear analyses of multilayer composites. II. Dynamics, *Computer Methods in Applied Mechanics and Engineering* 192 (9) (2003) 1017–1059. doi:10.1016/S0045-7825(02)00336-5.
- [11] K. Y. Sze, Three-dimensional continuum finite element models for plate/shell analysis, *Progress in Structural Engineering and Materials* 4 (4) (2002) 400–407. doi:10.1002/pse.133.
- [12] D. Magisano, L. Leonetti, G. Garcea, Advantages of the mixed format in geometrically nonlinear analysis of beams and shells using solid finite elements, *International Journal for Numerical Methods in Engineering* 109 (9) (2017) 1237–1262. doi:10.1002/nme.5322.
- [13] K. Y. Sze, L. Q. Yao, A hybrid stress ANS solid-shell element and its generalization for smart structure modelling. Part I—solid-shell element formulation, *International Journal for Numerical Methods in Engineering* 48 (4) (2000) 545–564. doi:10.1002/(SICI)1097-0207(20000610)48:4<545::AID-NME889>3.0.CO;2-6.
- [14] S. Reese, P. Wriggers, B. D. Reddy, A new locking-free brick element technique for large deformation problems in elasticity, *Computers & Structures* 75 (3) (2000) 291–304. doi:10.1016/S0045-7949(99)00137-6.
- [15] S. Reese, A large deformation solid-shell concept based on reduced integration with hourglass stabilization, *International Journal for Numerical Methods in Engineering* 69 (8) (2007) 1671–1716. doi:10.1002/nme.1827.
- [16] M. Schwarze, S. Reese, A reduced integration solid-shell finite element based on the EAS and the ANS concept—Geometrically linear problems, *International Journal for Numerical Methods in Engineering* 80 (10) (2009) 1322–1355. doi:10.1002/nme.2653.
- [17] M. Schwarze, S. Reese, A reduced integration solid-shell finite element based on the EAS and the ANS concept—Large deformation problems, *International Journal for Numerical Methods in Engineering* 85 (3) (2011) 289–329. doi:10.1002/nme.2966.
- [18] W. F. Mitchell, The hp-multigrid method applied to hp-adaptive refinement of triangular grids, *Numerical Linear Algebra with Applications* 17 (2-3) (2010) 211–228. doi:10.1002/nla.700.
- [19] M. Ainsworth, J. Coyle, Hierarchic finite element bases on unstructured tetrahedral meshes, *International Journal for Numerical Methods in Engineering* 58 (14) (2003) 2103–2130. doi:10.1002/nme.847.
- [20] I. Gradshteyn, I. Ryzhik, *Table of Integrals, Series, and Products*, 5th Edition, Academic Press, UK, 1994.
- [21] M. A. Crisfield, A consistent co-rotational formulation for non-linear, three-dimensional, beam-elements, *Computer Methods in Applied Mechanics and Engineering* 81 (2) (1990) 131–150. doi:10.1016/0045-7825(90)90106-V.
- [22] T. Belytschko, H. Stolarski, W. K. Liu, N. Carpenter, J. S. J. Ong, Stress projection for membrane and shear locking in shell finite elements, *Computer Methods in Applied Mechanics and Engineering* 51 (1) (1985) 221–258. doi:10.1016/0045-7825(85)90035-0.
- [23] X. S. Li, An Overview of SuperLU: Algorithms, Implementation, and User Interface, *ACM Trans. Math. Softw.* 31 (3) (2005) 302–325. doi:10.1145/1089014.1089017.
- [24] K. Y. Sze, X. H. Liu, S. H. Lo, Popular benchmark problems for geometric nonlinear analysis of shells, *Finite Elements in Analysis and Design* 40 (11) (2004) 1551–1569. doi:10.1016/j.finel.2003.11.001.



(a) Step 50 ($q = 0.064$)



(b) Step 150 ($q = 0.380$)



(c) Step 211 ($q = 0.8$)

Figure 14: Deformed shapes for the nonlinear analysis of slit annular plate at different stages of the analysis.

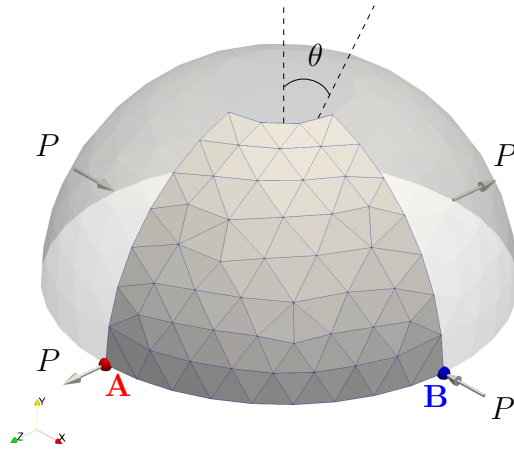


Figure 15: Geometry, mesh and loading of hemispherical shell

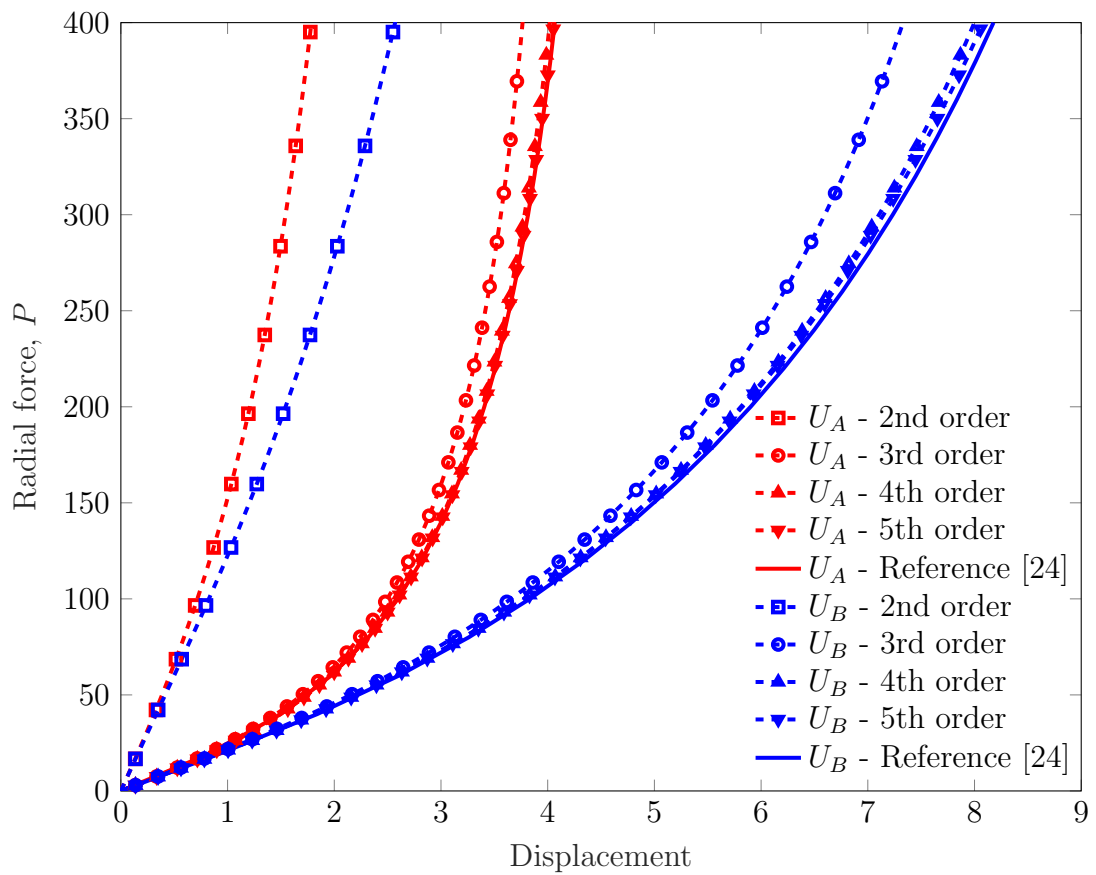
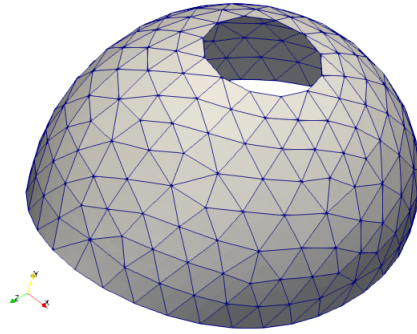
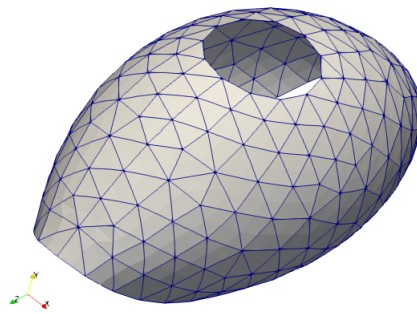


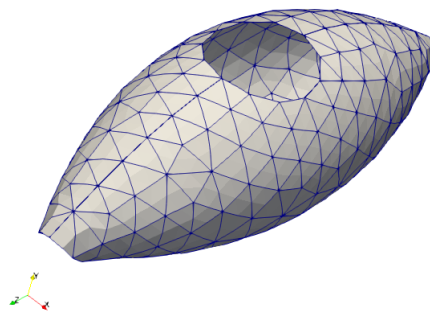
Figure 16: Comparison of radial displacements of hemispherical shell at points A (red) and B (blue) for different orders of approximation.



(a) Step 20 ($P = 32$)



(b) Step 70 ($P = 198$)



(c) Step 137 (last step, $P = 1,578$)

Figure 17: Deformed shapes of hemispherical shell at three different stages of the analysis.

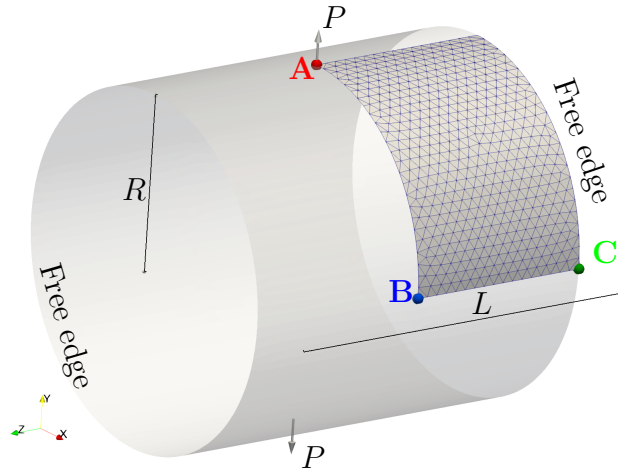


Figure 18: Geometry, boundary conditions, loading and mesh for the pull-out cylinder.

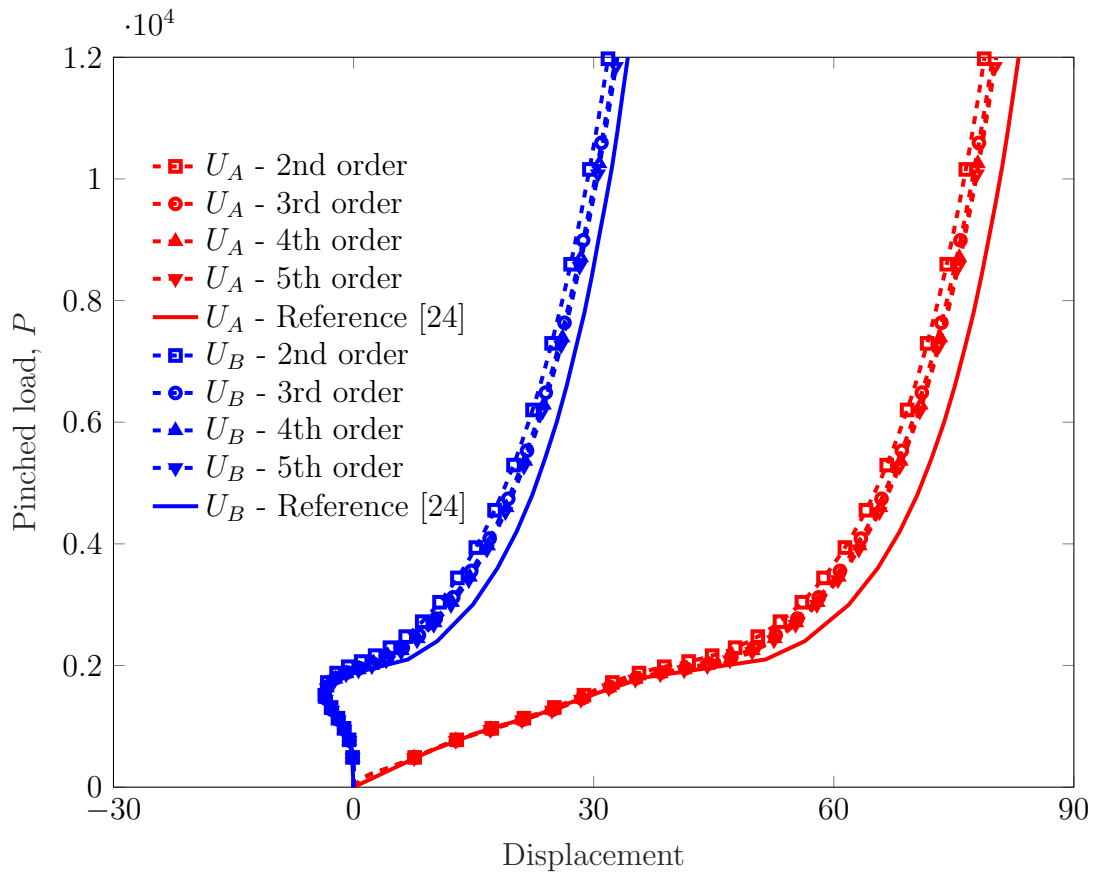
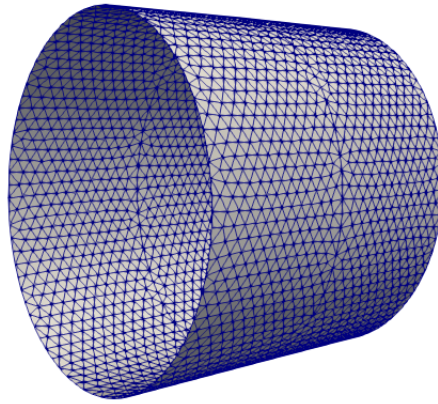
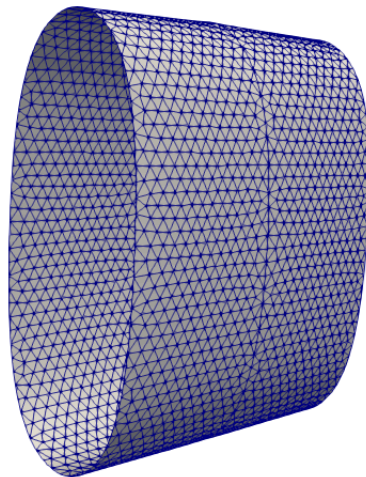


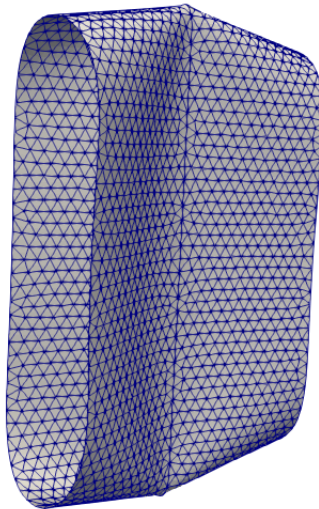
Figure 19: Comparison of radial displacements of the pull-out cylindrical shell at points A (red), B (blue), and C (green) for different orders of approximation.



(a) Step 10 ($P = 528$)



(b) Step 40 ($P = 3,671$)



(c) Step 87 (last step, $P = 52,414$)

Figure 20: Deformed shapes of the cylindrical shell at three different stages of the analysis.

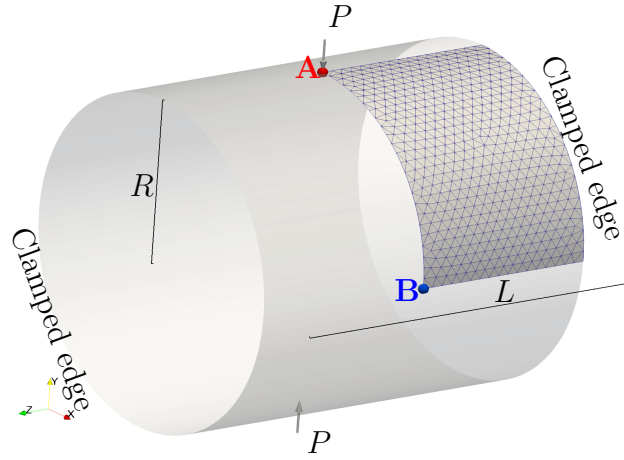


Figure 21: Geometry, boundary conditions, loading and mesh for pinched cylindrical shell with rigid diaphragms.

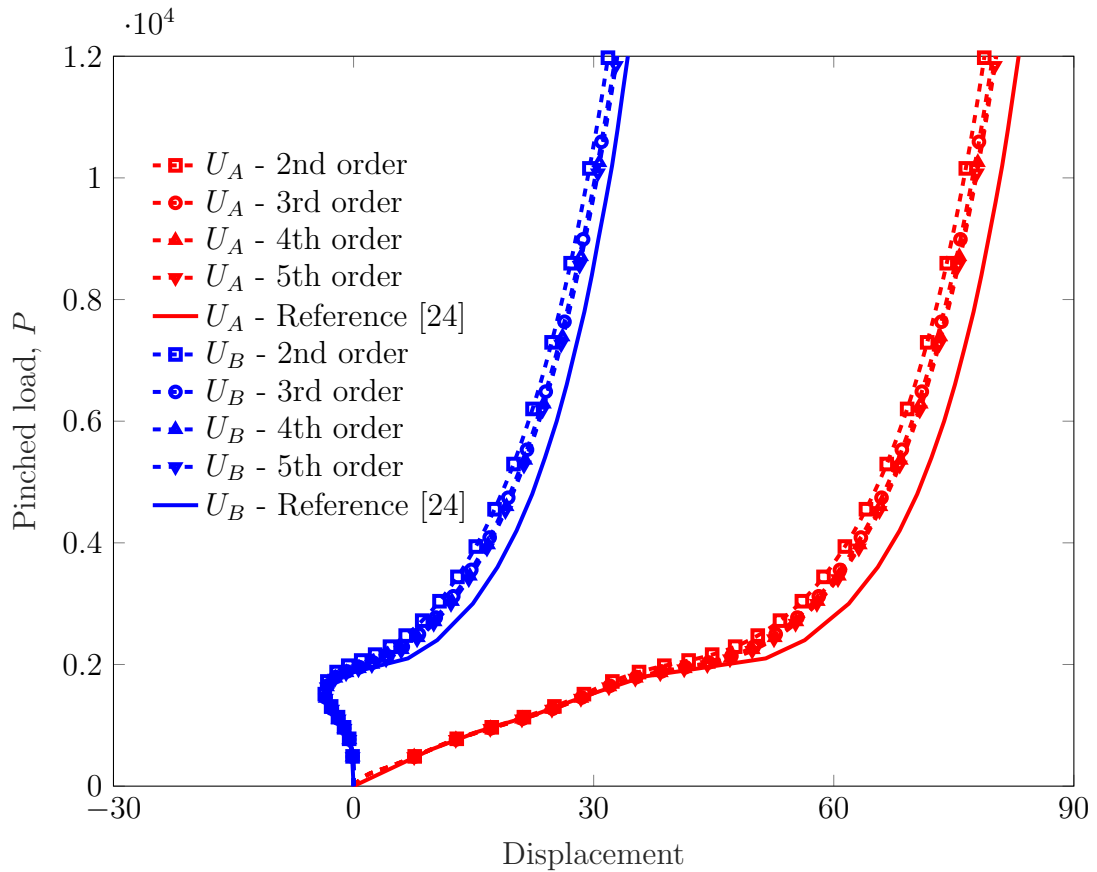
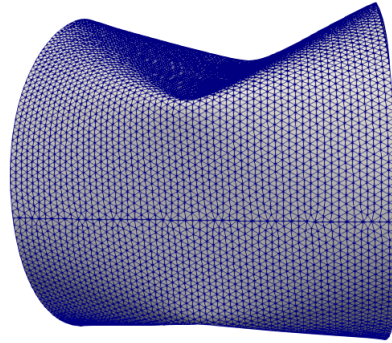
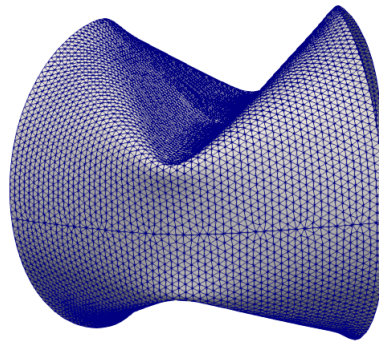


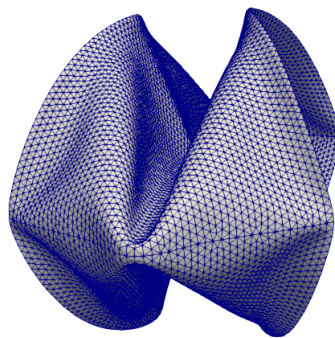
Figure 22: Comparison of radial displacements of the pinched shell at points A (red) and B (blue) for different orders of approximation.



(a) Step 100 ($P = 1,963$)



(b) Step 200 ($P = 5,620$)



(c) Step 368 (last step, $P = 48,529$)

Figure 23: Deformed shapes of the pinched cylindrical shell at three stages of the analysis.